

Non-intrusive uncertainty quantification

Jeroen A.S. Witteveen

Center for Mathematics and Computer Science (CWI)

Science Park 123

1098XG Amsterdam

The Netherlands

jeroen.witteveen@cw.nl

ABSTRACT

Numerical errors in Computational Fluid Dynamics (CFD) can already be made sufficiently small. Nowadays physical uncertainties tend to dominate the accuracy of numerical CFD predictions. In Uncertainty Quantification (UQ), the input uncertainties are taken into account by probability distributions. Deriving a new model for propagating the uncertainty using an intrusive UQ approach requires the modification of existing codes. An alternative is to use non-intrusive UQ methods, which can re-use an existing deterministic solver as a black-box. These kind of non-intrusive UQ methods interpolate samples in the range of the input distributions. However, this interpolation has the disadvantage that it can lead to overshoots of the samples in case of discontinuous responses, such as shock waves and contact surfaces. The unique contribution that CFD can bring to the field of UQ is the robust approximation of discontinuities in the probability space. There is extensive experience in the finite volume method (FVM) community with original robustness concepts for the reliable solution of these discontinuities. Here, we extend a number of these robustness principles to the probability space and demonstrate their effectiveness in test problems from stochastic CFD. The introduced concepts are: Local Extremum Conserving/Diminishing (LEC/LED) limiters; Total Variation Diminishing (TVD) schemes; Essentially Non-Oscillatory (ENO) stencil selection; Subcell resolution (SR); and Monotonicity Preserving (MP) limiters.

Contents

1.0 Introduction	2
2.0 Methodology	3
2.1 Simplex Stochastic Collocation	3
2.2 ENO stencil selection	5
2.3 Subcell resolution	8
2.4 Monotonicity preserving limiter	10
3.0 Results	11
3.1 Shock tube problem	11
3.2 Transonic airfoil	15
3.2.1 Inviscid flow	15

3.2.2 Viscous flow	18
------------------------------	----

4.0 Conclusions	19
------------------------	-----------

1.0 INTRODUCTION

Computational Fluid Dynamics (CFD) is the process in which real-world objects or designs are described by a geometrical representation in a computer to predict the forces of the fluid on the object using a discretization of the space around the object. In this process, numerical errors are introduced in the form of the finite discretization error, the approximation order truncation error, the nonlinear iteration error, and the digital computer round-off error. However, numerical error estimation is a well-established field and computational resources are nowadays so widely available that these numerical errors can be made sufficiently small. On the other hand, also physical uncertainties have an impact CFD predictions. These can be weather conditions through the boundary conditions, production tolerances on the geometry, wear and tear of the surface roughness parameter, and model-form uncertainty. Nowadays these physical uncertainties tend to dominate the accuracy of numerical CFD predictions.

The common deterministic simulation paradigm is to assume that model parameters, and initial and boundary conditions are exactly known. The model then results in one prediction for the output quantities of interest. In Uncertainty Quantification (UQ), the input uncertainties can be taken into account by probability distributions. The objective of UQ is then to compute the probability distribution and the statistical moments of the outputs of interest. These uncertainties can be propagated by deriving a new model and implementation for the uncertainty propagation problem, which can be solved at once. This is called intrusive UQ, because existing deterministic codes need to be modified.

An alternative is to use non-intrusive UQ methods, which can re-use an existing deterministic solver as a black-box. These kind of methods are based on performing multiple deterministic simulations for the parameter values in the range of the uncertain input distributions. The Monte Carlo (MC) simulation method is one of these non-intrusive UQ methods and it is based on collecting ensemble statistics of many simulations for randomly sampled parameter values. In order to reduce the number of CFD runs to a feasible level, other non-intrusive UQ methods employ a form of interpolation of the sampling results. One of such methods is the Stochastic Collocation (SC) method, which is based on Lagrangian global polynomial interpolation of sampling at numerical quadrature points. However, this interpolation has the disadvantage that it can lead to overshoots of the samples and non-zero probabilities for unphysical predictions in case of discontinuous responses, which can occur in the solution of the nonlinear equations governing fluid flow in the form of shock waves and contact surfaces.

The unique contribution that CFD can bring to the field of UQ is the robust approximation of discontinuities in the probability space. There is extensive experience in the finite volume method (FVM) community with original robustness concepts for the reliable solution of discontinuities in the form of shock waves and contact surfaces in flow fields. Here, we extend a number of these robustness principles to the probability space and demonstrate their effectiveness in test problems from stochastic CFD. The introduced concepts are:

1. Local Extremum Conserving/Diminishing (LEC/LED) limiters;
2. Total Variation Diminishing (TVD) schemes;
3. Essentially Non-Oscillatory (ENO) stencil selection;
4. Subcell resolution (SR);

5. Monotonicity Preserving (MP) limiters.

These approaches are implemented into the multi-element Simplex Stochastic Collocation (SSC) UQ method in the next section. They can also be applied to other UQ methodologies. Abgrall [1] and Barth [2] have extended FVM directly to discretize the combined physical and probability spaces using the ENO scheme. We consider here the spatial and stochastic dimensions separately to reduce the dimensionality of the problems. Subcell resolution in stochastic methods has also been proposed by Ghosh and Ghanem [4] in the form of basis enrichment in the polynomial chaos expansion. Their approach is, however, based on incorporating *a priori* knowledge about the discontinuity location by selecting appropriate enrichment functions. A solution for the staircase approximation of the statistics in case of random spatial discontinuities has also been proposed by Barth [2] using image enhancement postprocessing techniques in the combined discretization of the physical and probability spaces. The conclusions from the numerical results in Section 3.0 are summarized in Section 4.0.

2.0 METHODOLOGY

Consider the following computationally intensive problem subject to n_ξ second-order random parameters $\xi = \{\xi_1, \dots, \xi_{n_\xi}\} \subset \Xi$ with a known input probability density $f_\xi(\xi)$ in the parameter space $\Xi \subset \mathbb{R}^{n_\xi}$

$$\mathcal{L}(\mathbf{x}, t, \xi; u(\mathbf{x}, t, \xi)) = \mathcal{S}(\mathbf{x}, t, \xi). \quad (1)$$

where the operator \mathcal{L} and the source term \mathcal{S} are defined on the domain $X \times T \times \Xi$ with output quantity of interest $u(\mathbf{x}, t, \xi)$, space $\mathbf{x} \in X \subset \mathbb{R}^{n_x}$, $n_x = \{1, 2, 3\}$, and time $t \in T \subset \mathbb{R}$. The latter two arguments are dropped to simplify the notation. Second-order random parameters are random parameters with finite variance, which includes most practical cases [3]. The solution of (1) is a random event with the set of outcomes Ω of the probability space (Ω, \mathcal{F}, P) with $\mathcal{F} \subset 2^\Omega$ the σ -algebra of events and P a probability measure.

2.1 Simplex Stochastic Collocation

The SSC method with the stencil selection and subcell resolution extensions are of the multi-element type of UQ methods. Multi-element UQ methods discretize the stochastic dimensions using multiple subdomains comparable to spatial discretizations in physical space. These local methods [8] can be based on Stochastic Galerkin (SG) projections of Polynomial Chaos (PC) expansions [3] in each of the subdomains. Other methods use a Stochastic Collocation (SC) approach [16] to construct the local polynomial approximations based on sampling at quadrature points in the elements. These methods commonly use sparse grids of Gauss quadrature rules in hypercube subdomains combined with solution-based refinement measures for resolving nonlinearities. Because of the hypercube elements, these methods are most effective in capturing discontinuities that are aligned with one of the stochastic coordinates.

The simplex stochastic collocation (SSC) method [12, 13] computes the statistics and the probability distribution of $u(\xi)$ in a non-intrusive way by discretizing the probability space using a simplex tessellation of n_s samples points ξ_k , with $k = 1, \dots, n_s$. This is a similar concept to spatial discretizations of the physical space in CFD methods. A series of n_s deterministic problems (1) is then solved to compute the samples $\mathbf{v} = \{v_1, \dots, v_{n_s}\}$, with $v_k = u(\xi_k)$, for the parameter values ξ_k that correspond to the vertexes of the n_e simplexes Ξ_j in probability space with $j = 1, \dots, n_e$. The response surface $u(\xi)$ is approximated by a piecewise polynomial interpolation $w(\xi)$ of the samples \mathbf{v} using a polynomial chaos [3] expansion $w_j(\xi)$ in each of the

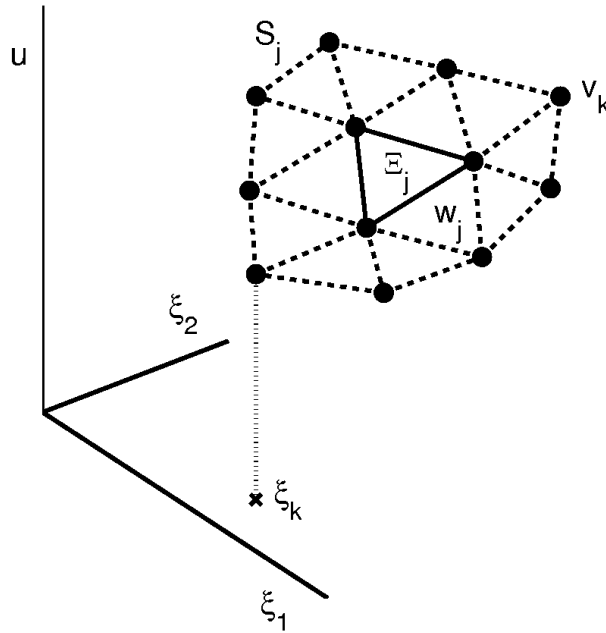


Figure 1: Approximation of the response surface $u(\xi)$ by the interpolation $w_j(\xi)$ of the samples v_k at a stencil S_j of sampling points ξ_k for the simplex Ξ_j in a two-dimensional probability space with $\xi = \{\xi_1, \xi_2\}$.

simplexes Ξ_j

$$w_j(\xi) = \sum_{i=0}^{P_j} c_{j,i} \Psi_{j,i}(\xi), \quad (2)$$

for $\xi \in \Xi_j$, where $\Psi_{j,i}$ are the basis polynomials, $c_{j,i}$ are the coefficients, and $P_j + 1 = (n_\xi + p_j)! / (n_\xi! p_j!)$ is the number of expansion terms, with p_j the local polynomial degree of $w_j(\xi)$. The coefficients $c_{j,i}$ are computed by interpolating a stencil S_j out of the n_s samples $\mathbf{v} = \{v_1, \dots, v_{n_s}\}$. For a piecewise linear interpolation $w_j(\xi)$ with $p_j = 1$, the stencil $S_j = \{\xi_{k_{j,0}}, \dots, \xi_{k_{j,N_j}}\}$ consists of the $N_j + 1 = n_\xi + 1$ vertexes of the simplex Ξ_j , with $k_{j,l} \in \{1, \dots, n_s\}$ for $j = 1, \dots, n_e$ and $l = 0, \dots, N_j$. Higher degree stencils S_j with $N_j \geq P_j$ are constructed by adding vertexes ξ_k of surrounding simplexes to the stencil according to a nearest neighbor search based on the Euclidean distance to the center of the simplex Ξ_j in parameter space Ξ . The center of Ξ_j is defined as the average of the vertex locations of Ξ_j . The relation $N_j = P_j$ is used here or least squares approximation can be used to construct the interpolation for $N_j > P_j$. The interpolation procedure (2) in the probability space is denoted by the interpolation operator \mathcal{I} , for which holds $w(\mathbf{x}, \xi) = \mathcal{I}(\mathbf{v}(\mathbf{x}))$. The notation is visualized in Figure 1 for an example of a response surface approximation in a two-dimensional probability space with $n_\xi = 2$.

The polynomial degree p_j is chosen as high as possible with respect to the total number of available samples n_s with $N_j + 1 \leq n_s$. The robustness of the interpolation $w_j(\xi)$ of the samples $\mathbf{v}_j = \{v_{k_{j,0}}, \dots, v_{k_{j,n_\xi}}\}$ in the simplex Ξ_j is guaranteed by the local extremum conserving (LEC) limiter that reduces the stencil size $N_j + 1$, and p_j , in case of overshoots until $w_j(\xi)$ satisfies

$$\min_{\xi \in \Xi_j} w_j(\xi) = \min \mathbf{v}_j \wedge \max_{\xi \in \Xi_j} w_j(\xi) = \max \mathbf{v}_j. \quad (3)$$

The LEC limiter (3) is applied to all simplexes in a stencil S_j and always holds for $p_j = 1$. The resulting interpolation $w(\boldsymbol{\xi})$ is then Local Extremum Diminishing (LED) with respect to the exact but unknown solution $u(\boldsymbol{\xi})$. The i th moment μ_{u_i} of $u(\boldsymbol{\xi})$ is then computed as a summation of integrals over the n_e simplexes Ξ_j using a Monte Carlo evaluation with $n_{mc} \gg n_s$ integration points $\boldsymbol{\xi}_{mc_k}$

$$\mu_{u_i}(\mathbf{x}) \approx \sum_{j=1}^{n_e} \int_{\Xi_j} w_j(\mathbf{x}, \boldsymbol{\xi})^i f_{\xi}(\boldsymbol{\xi}) d\boldsymbol{\xi} \approx \sum_{k=1}^{n_{mc}} w(\mathbf{x}, \boldsymbol{\xi}_{mc_k})^i, \quad (4)$$

with $w(\mathbf{x}, \boldsymbol{\xi}_{mc_k}) = w_j(\mathbf{x}, \boldsymbol{\xi}_{mc_k})$ for $\boldsymbol{\xi}_{mc_k} \in \Xi_j$.

The initial discretization of the probability space consists of a simplex tessellation of sampling points $\boldsymbol{\xi}_k$ at the corners of a hypercube probability space and one sample in the interior. The sampling strategy is then based on splitting the longest edge of the simplex Ξ_j with the highest value of a refinement measure in each refinement step in two by adding a sampling point $\boldsymbol{\xi}_k$. The random sampling point is located at least one third of the edge length away from the endpoints to ensure a sufficient spread of the samples. In a one-dimensional probability space, the new sampling point $\boldsymbol{\xi}_k$ is used to split the cell Ξ_j into two cells of equal size. The tessellation is updated by computing the sample $v_{k_{new}} = u(\boldsymbol{\xi}_{k_{new}})$ and by making a Delaunay triangulation of the new set of sampling points $\boldsymbol{\xi}_k$ or by splitting the simplexes Ξ_j that contain the refined edge in two. The following refinement measure e_j is used based on the geometrical properties of the simplex Ξ_j and the local polynomial degree p_j

$$e_j = \bar{\Omega}_j \bar{\Xi}_j^{2O_j}, \quad (5)$$

where the probability $\bar{\Omega}_j$, the normalized volume $\bar{\Xi}_j$, and the estimated order of convergence O_j of Ξ_j are defined as

$$\bar{\Omega}_j = \int_{\Xi_j} f_{\xi}(\boldsymbol{\xi}) d\boldsymbol{\xi}, \quad \bar{\Xi}_j = \frac{1}{\Xi} \int_{\Xi_j} d\boldsymbol{\xi}, \quad O_j = \frac{p_j + 1}{n_{\xi}}, \quad (6)$$

with $\Xi = \sum_{j=1}^{n_e} \bar{\Xi}_j$. Measure (5) accounts for both the interpolation accuracy and the probabilistic weighting in the moment integrals (4). It also leads to solution-based refinement through the reduction of p_j at discontinuities by the LEC limiter (3). The size $\bar{\Xi}_j$ of the simplexes can be used as the refinement measure in order to obtain uniform or volumetric refinement.

2.2 ENO stencil selection

The ENO spatial discretization [5] achieves an essentially non-oscillatory approximation of the solution of hyperbolic conservation laws. Non-oscillatory means, in this context, that the number of local extrema in the solution does not increase with time. The ENO scheme obtains this property using an adaptive-stencil approach with a uniform polynomial degree for reconstructing the spatial fluxes. Each spatial cell X_j is assigned r stencils $\{S_{j,i}\}_{i=1}^r$ of degree p , all of which include the cell X_j itself. Out of this set of candidate stencils $\{S_{j,i}\}$, the stencil S_j is selected for cell X_j that results in the interpolation $w_j(\mathbf{x})$ which is smoothest in some sense based on an indicator of smoothness $IS_{j,i}$. In this way, a cell next to a discontinuity is adaptively given a stencil consisting of the smooth part of the solution, which avoids Gibbs-like oscillations in physical space. Attention has been paid to the efficient implementation of ENO schemes by Shu and Osher [9].

The nearest neighbor construction of the interpolation stencils S_j combined with the LEC limiter (3) results in one stencil S_j for each simplex Ξ_j . If the stencils S_j are not restricted to the nearest neighbor sampling points $\boldsymbol{\xi}_k$, then multiple stencils $S_{j,i}$ may be possible for simplex Ξ_j that satisfy the LEC limiter. The stencil $S_{j,i}$ that leads to the smoothest interpolation $w_{j,i}(\boldsymbol{\xi})$ is then selected for a more accurate approximation of $u(\boldsymbol{\xi})$ [14].

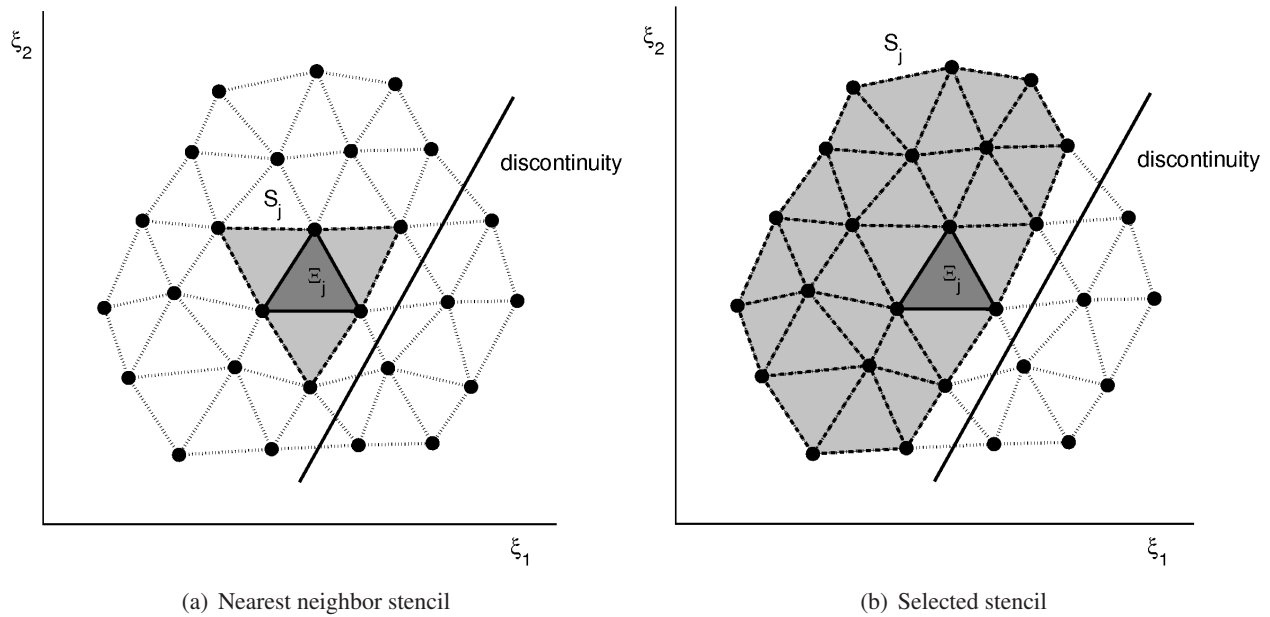


Figure 2: Selection of the interpolation stencil S_j for the simplex Ξ_j near a discontinuity in a two-dimensional probability space.

The first $n_\xi + 1$ sampling points ξ_k of each stencil $S_{j,i} = \{\xi_{k_{j,0}}, \dots, \xi_{k_{j,n_\xi}}\}$ consist of the vertices of the simplex Ξ_j . This stencil corresponds to the piecewise linear interpolation. The higher degree stencils of $N_{j,i} + 1$ sampling points

$$S_{j,i} = \{\xi_{k_{j,0}}, \dots, \xi_{k_{j,n_\xi}}, \dots, \xi_{k_{j,N_{j,i}}}\}, \quad (7)$$

can be constructed by adding, in principle, any combination of $N_{j,i} - n_\xi$ samples for any $p_{j,i}$ out of the remaining sampling points ξ_k , with $k \in \{1, \dots, n_s\} \setminus \{k_{j,0}, \dots, k_{j,n_\xi}\}$ and each sampling point appearing only once in the stencil $S_{j,i}$. Out of these stencils, only a set of r_j candidate stencils $\{S_{j,i}\}_{i=1}^{r_j}$ is accepted of which the interpolation $w_{j,i}(\xi)$ satisfies the LEC limiter. The stencil S_j for Ξ_j is selected from this set $\{S_{j,i}\}$ based on an indicator of smoothness $IS_{j,i}$ for each of the candidates. Since the stencils $S_{j,i}$ have a non-uniform polynomial degree $p_{j,i}$, the degree of the stencils accepted by the LEC limiter is here used as the indicator of smoothness $IS_{j,i} = p_{j,i}$. The stencil with the highest polynomial degree is then assigned to Ξ_j in order to obtain the highest order approximation

$$S_j = S_{j,i}, \quad \text{with } i = \arg \max_{i^* \in \{1, \dots, r_j\}} p_{j,i^*}. \quad (8)$$

If multiple stencils have the same smoothness $p_{j,i}$, then out of these stencils the one with the minimum average Euclidean distance of the sampling points ξ_k to the center of Ξ_j is chosen.

A two-dimensional example is given in Figure 2 of the stencil selection for the simplex Ξ_j close to a discontinuity, of which the location is denoted by the diagonal line. The nearest neighbor stencil S_j for Ξ_j only leads to a quadratic interpolation $w_j(\xi)$ with $N_j + 1 = 6$, since higher degree stencils cross the discontinuity and are rejected by the LEC limiter. On the other hand, stencil selection can result in a stencil S_j , with a higher polynomial degree p_j , that contains all sampling points ξ_k in the smooth region at one side of the discontinuity.

Constructing all possible stencils $S_{j,i}$ for all simplexes Ξ_j can become impractical as its complexity increases binomially with the number of samples n_s . Therefore, we restrict the stencil selection to a subset of these stencils by employing the multi-element character of the approach. We allow only nearest neighbor sten-

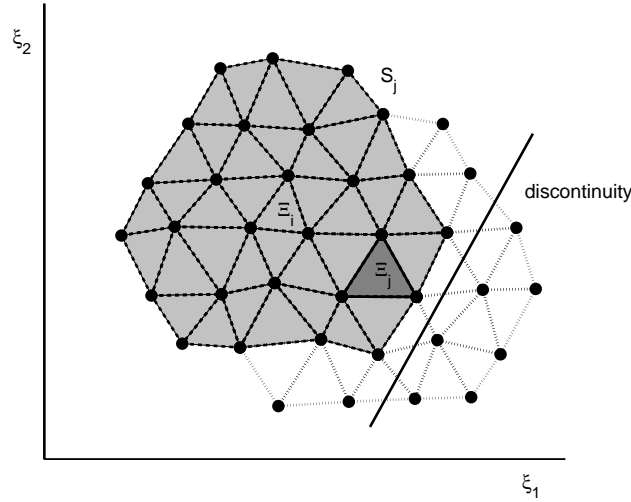


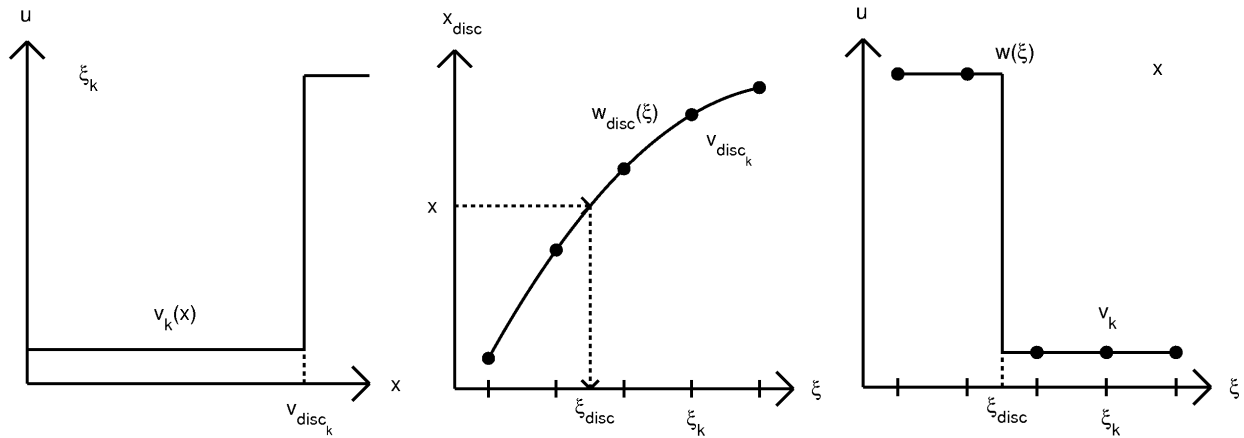
Figure 3: Efficiently selected stencil S_j for the simplex Ξ_j by adopting the nearest neighbor stencil of the simplex Ξ_i in a two-dimensional probability space.

cils of other simplexes that contain Ξ_j to be assigned to the simplex Ξ_j , if that leads to a higher polynomial degree than its own stencil.

To that end, the nearest neighbor stencils \tilde{S}_j , with interpolation $\tilde{w}_j(\boldsymbol{\xi})$ and degree \tilde{p}_j , are first constructed for each simplex Ξ_j as described in Section 2.1. This results in a set of n_e stencils $\{\tilde{S}_j\}_{j=1}^{n_e}$ for all simplexes Ξ_j . Next, it needs to be determined for each stencil \tilde{S}_j which simplexes Ξ_i are part of the stencil. A stencil \tilde{S}_j is considered to contain another simplex Ξ_i , if \tilde{S}_j contains all vertexes $\{\boldsymbol{\xi}_{k_{i,0}}, \dots, \boldsymbol{\xi}_{k_{i,n_\xi}}\}$ of Ξ_i , which is always true for $i = j$. A set of \tilde{r}_j candidate stencils $\{\tilde{S}_{j,i}\}_{i=1}^{\tilde{r}_j}$ for simplex Ξ_j is then collected from the nearest neighbor stencils that contain Ξ_j . The stencil $S_j = \tilde{S}_{j,i}$, and the interpolation $w_j(\boldsymbol{\xi}) = \tilde{w}_{j,i}(\boldsymbol{\xi})$, with the highest degree $\tilde{p}_{j,i}$ is selected from $\{\tilde{S}_{j,i}\}_{i=1}^{\tilde{r}_j}$ as in (8). If none of the stencils $\{\tilde{S}_{j,i}\}$ has a higher degree than the nearest neighbor stencil \tilde{S}_j , i.e. $\tilde{p}_{j,i} \leq \tilde{p}_j$ for all $i = 1, \dots, \tilde{r}_j$, then the original stencil \tilde{S}_j is automatically maintained, since the sampling points of the nearest neighbor stencil have, by definition, the smallest average Euclidean distance to the center of Ξ_j .

This efficient SSC–ENO stencil selection algorithm results in virtually no additional computational costs compared to SSC with nearest neighbor stencils, since no additional stencils or interpolations are constructed. Existing nearest neighbor stencils are assigned only to other simplexes, if that increases the local polynomial degree. The algorithm can, therefore, only improve the polynomial degree, $p_j \geq \tilde{p}_j$, because $\{\tilde{S}_{j,i}\}$ always contains the stencil \tilde{S}_j . The impact of the stencil selection on the increase of the polynomial degree p_j in the smooth regions of the solution, decreases the refinement measure e_j in the simplexes in which the solution is smooth, since $\bar{\Xi}_j < 1$. This results in more focused refinement of the simplexes that contain nonlinearities.

Figure 3 shows the adoption of the nearest neighbor stencil of another simplex Ξ_i by the simplex Ξ_j in the two-dimensional example. Because the resulting stencil S_j is asymmetrical with respect to Ξ_j , it leads to a higher polynomial degree p_j than its nearest neighbor stencil of Figure 2(a). The efficiently selected stencil does not necessarily contain all the sampling points on one side of the discontinuity.



(a) Extraction \mathcal{E} of v_{disc_k} from the sample $v_k(x) = u(x, \xi_k)$ for the sampling point ξ_k (b) Intersection of $x_{disc}(\xi) = x$ with the interpolation $w_{disc}(\xi)$ of \mathbf{v}_{disc} at ξ_{disc} (c) Reconstruction of $w(\xi)$ with a discontinuity at ξ_{disc} for the physical location x

Figure 4: Example of the subcell resolution approach for a discontinuity in a one-dimensional probability space.

2.3 Subcell resolution

The notion of subcell resolution in FVM originated from Harten [6] to prevent the smearing of contact discontinuities in the solution of hyperbolic conservation laws in the physical space X . It is based on the observation that the location of a discontinuity x_{disc} within a spatial cell X_j can be derived from the computed cell-averaged value \bar{w}_j approximating a flow quantity $u(x)$. In an ENO scheme [5], the ENO reconstructions of $u(x)$ in the cells to the left and the right of the discontinuous cell X_j , $w_{j-1}(x)$ and $w_{j+1}(x)$, are then extended up to an approximation of the discontinuity location x_{disc} in X_j such that their integral matches the cell average \bar{w}_j . This allows for resolving discontinuities in the interior of the cells instead of restricting them to the cell face locations. The concept can be extended to multiple spatial dimensions using the dimensional splitting approach.

The subcell resolution is first introduced for a one-dimensional physical space $x \in X$ with $n_x = 1$ and later described for multiple spatial dimensions [15]. Assume that $u(x, \xi)$ contains a discontinuity, of which the location $x_{disc}(\xi)$ in the physical space X is a function of the stochastic dimensions ξ . The samples $\mathbf{v}(x)$ for the flow quantity $u(x, \xi)$ are then used to extract n_s realizations $\mathbf{v}_{disc} = \{v_{disc_1}, \dots, v_{disc_{n_s}}\}$ for the physical discontinuity location $x_{disc}(\xi)$ at the sampling points ξ_k . This is referred to as the extraction operation \mathcal{E} that returns $\mathbf{v}_{disc} = \mathcal{E}(\mathbf{v}(x))$ with $v_{disc_k} = x_{disc}(\xi_k)$. In Figure 4(a), an example of the extraction of v_{disc_k} from the sample $v_k(x)$ for the sampling point ξ_k is given for one stochastic dimension ξ . The set of realizations v_{disc_k} for $n_s = 5$ sampling points ξ_k is shown in Figure 4(b) by the dots in the plot of the discontinuity location $x_{disc}(\xi)$ in the physical space as function of the random parameter ξ .

The specific method for the extraction \mathcal{E} of the physical discontinuity locations v_{disc_k} from the deterministic flow fields for the local flow quantity $v_k(x)$ can depend on the type of representation of the discontinuity that is used by the spatial discretization method. The discontinuity locations are explicitly resolved, for example, in subcell resolution FVM discretizations in the physical space and front tracking methods or level set approaches. Shock sensors in hybrid shock capturing methods or adaptive mesh refinement strategies can also be used to identify the discontinuity locations. Otherwise, approaches can be used based on local maxima in the gradient magnitude of the solutions $v_k(x)$, such as the shock detector proposed by Harten [6].

The realizations \mathbf{v}_{disc} for the physical discontinuity location are interpolated over the probability space to

the function $w_{\text{disc}}(\boldsymbol{\xi})$ to obtain an approximation of the discontinuity location $x_{\text{disc}}(\boldsymbol{\xi})$ in the physical space as function of the stochastic coordinates $\boldsymbol{\xi}$, see Figure 4(b). The piecewise higher-degree polynomial interpolation $w_{\text{disc}}(\boldsymbol{\xi}) = \mathcal{I}(\mathbf{v}_{\text{disc}})$ is obtained using the interpolation operator \mathcal{I} (2)

$$w_{\text{disc}_j}(\boldsymbol{\xi}) = \sum_{i=0}^{P_{\text{disc}_j}} c_{\text{disc}_j,i} \Psi_{j,i}(\boldsymbol{\xi}), \quad (9)$$

with $w_{\text{disc}}(\boldsymbol{\xi}) = w_{\text{disc}_j}(\boldsymbol{\xi})$ for $\boldsymbol{\xi} \in \Xi_j$ and the $P_{\text{disc}_j} + 1$ coefficients $c_{\text{disc}_j,i}$ determined by the interpolation of a stencil S_{disc_j} of the realizations v_{disc_k} . The location of the discontinuity in the probability space for a certain point x in the physical space can then be described by the hypersurface $\Xi_{\text{disc}}(x) \subset \Xi$. This discontinuous hypersurface $\Xi_{\text{disc}}(x)$ in the probability space is given by the intersection of $w_{\text{disc}}(\boldsymbol{\xi})$ with the hyperplane $x_{\text{disc}}(\boldsymbol{\xi}) = x$, such that for all points $\boldsymbol{\xi}_{\text{disc}} \in \Xi_{\text{disc}}(x)$ holds $w_{\text{disc}}(\boldsymbol{\xi}_{\text{disc}}) = x$. Therefore, Ξ_{disc} contains all combinations of random parameter values $\boldsymbol{\xi}_{\text{disc}}$ for which the discontinuity in the physical space is predicted to be located at x . In the example of Figure 4(b) with a one-dimensional probability space, the set $\Xi_{\text{disc}}(x)$ consists of a single point ξ_{disc} for which $w_{\text{disc}}(\xi_{\text{disc}}) = x$. For multiple random parameters $\boldsymbol{\xi}$, the intersection $\Xi_{\text{disc}}(x)$ of $w_{\text{disc}}(\boldsymbol{\xi})$ with $x_{\text{disc}}(\boldsymbol{\xi}) = x$ is a piecewise higher-degree function that is able to capture nonlinear curvatures of discontinuous hypersurfaces in the probability space.

The parameter space Ξ is next divided into two subdomains $\Xi^-(x)$ and $\Xi^+(x)$ separated by $\Xi_{\text{disc}}(x)$, for which holds $w_{\text{disc}}(\boldsymbol{\xi}^-) < x$ with $\boldsymbol{\xi}^- \in \Xi^-(x)$, $w_{\text{disc}}(\boldsymbol{\xi}^+) > x$ with $\boldsymbol{\xi}^+ \in \Xi^+(x)$, and $\Xi = \Xi^-(x) \cup \Xi^+(x)$. The discontinuous simplexes Ξ_j that contain $\Xi_{\text{disc}}(x)$ are identified by

$$w_{\text{disc}_j}(\boldsymbol{\xi}^-) < x \text{ for some } \boldsymbol{\xi}^- \in \Xi_j \wedge w_{\text{disc}_j}(\boldsymbol{\xi}^+) > x \text{ for some } \boldsymbol{\xi}^+ \in \Xi_j. \quad (10)$$

The interpolation $w_j(x, \boldsymbol{\xi})$ (2), in the simplexes Ξ_j that satisfy (10), is replaced by a discontinuous representation of the response surface $u(x, \boldsymbol{\xi})$. To that end, the simplex Ξ_j is divided into two regions $\Xi_j^-(x) \subset \Xi^-(x)$ and $\Xi_j^+(x) \subset \Xi^+(x)$ with $\Xi_j = \Xi_j^-(x) \cup \Xi_j^+(x)$. The interpolation $w_j(x, \boldsymbol{\xi})$ in $\Xi_j^-(x)$ is replaced by the approximation $w_j^-(x, \boldsymbol{\xi}) = w_{i^-}(x, \boldsymbol{\xi})$ of the simplex Ξ_{i^-} closest to Ξ_j for which holds $\Xi_{i^-} \subset \Xi^-$. The nearest cell Ξ_{i^-} is defined as the simplex that has the most vertexes $\boldsymbol{\xi}_k$ in common with Ξ_j and that has the highest polynomial degree p_{i^-} out of these cells. The region $\Xi_j^+(x)$ is assigned the different interpolation $w_j^+(x, \boldsymbol{\xi}) = w_{i^+}(x, \boldsymbol{\xi})$ of the nearest simplex $\Xi_{i^+} \subset \Xi^+$ with $i^-, i^+ \in \{1, \dots, n_e\}/j$. The notation is illustrated in Figure 5 for the case of a two-dimensional probability space. This leads for SSC–SR to the response surface approximation $w(x, \boldsymbol{\xi})$ given by

$$w(x, \boldsymbol{\xi}) = \begin{cases} w_j(x, \boldsymbol{\xi}), & \boldsymbol{\xi} \in \Xi_j, \quad \Xi_j \subset \Xi^- \vee \Xi_j \subset \Xi^+, \\ w_j^-(x, \boldsymbol{\xi}), & \boldsymbol{\xi} \in \Xi_j^-, \quad \Xi_j \not\subset \Xi^- \wedge \Xi_j \not\subset \Xi^+, \\ w_j^+(x, \boldsymbol{\xi}), & \boldsymbol{\xi} \in \Xi_j^+, \quad \Xi_j \not\subset \Xi^- \wedge \Xi_j \not\subset \Xi^+, \end{cases} \quad (11)$$

which is discontinuous at the predicted discontinuity location $\Xi_{\text{disc}}(x)$, see Figure 4(c) for the result in the one-dimensional probability space. Integrating $w(x, \boldsymbol{\xi})$ over the parameter space Ξ yields an approximation of the statistical moments of u at the spatial point x . In order to obtain the spatial fields for the mean $\mu_w(x)$ and the standard deviation $\sigma_w(x)$, the approximations $\Xi_{\text{disc}}(x)$ and $w(x, \boldsymbol{\xi})$ are constructed for each point x in the spatial discretization of X .

In multiple spatial dimensions, $n_x \in \{2, 3\}$, the location of the discontinuity is described by the discontinuous surface $X_{\text{disc}}(\boldsymbol{\xi}) \subset X$ in the physical space. Therefore, instead of using the discontinuity location $x_{\text{disc}}(\boldsymbol{\xi})$, the signed Euclidean distance $d_{\text{disc}}(\mathbf{x}, \boldsymbol{\xi})$ from the discontinuity $X_{\text{disc}}(\boldsymbol{\xi})$ to a point \mathbf{x} in the physical space is parameterized for $n_x > 1$. The sign is obtained using the cross product, at the point on the discontinuity $X_{\text{disc}}(\boldsymbol{\xi})$ closest to \mathbf{x} , between the tangent of $X_{\text{disc}}(\boldsymbol{\xi})$ and the vector to \mathbf{x} , which is illustrated in Section 3.2.1

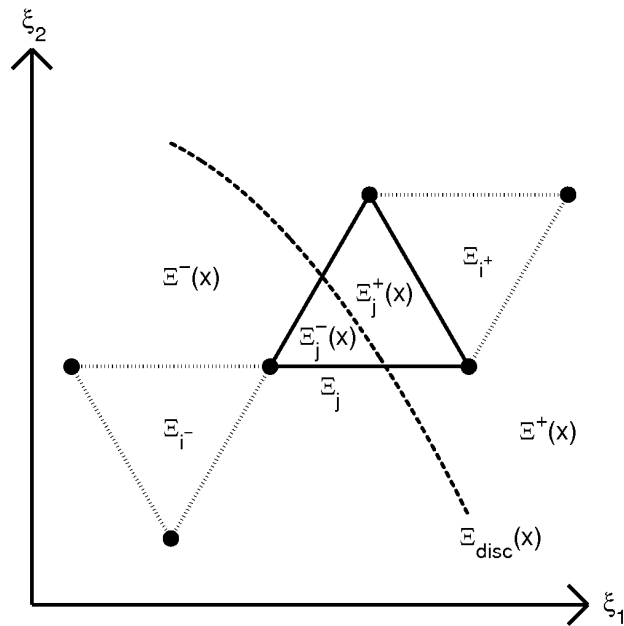


Figure 5: Division of the simplex Ξ_j in the two-dimensional parameter space Ξ by the discontinuous front $\Xi_{\text{disc}}(x)$ into $\Xi_j^-(x)$ and $\Xi_j^+(x)$ with the nearest simplexes Ξ_{i-} and Ξ_{i+} in $\Xi^-(x)$ and $\Xi^+(x)$, respectively.

for the RAE 2822 airfoil. The subcell resolution method is then equal to the approach presented in this section for $n_x = 1$ by substituting $d_{\text{disc}}(\mathbf{x}, \boldsymbol{\xi})$ for $x_{\text{disc}}(\boldsymbol{\xi})$ and the location of the discontinuous hypersurface $\Xi_{\text{disc}}(\mathbf{x})$ is given by $d_{\text{disc}}(\mathbf{x}, \boldsymbol{\xi}) = 0$. Since $d_{\text{disc}}(\mathbf{x}, \boldsymbol{\xi})$ depends on the reference point \mathbf{x} in the physical space, the realizations $v_{\text{disc}_k}(\mathbf{x})$ of $d_{\text{disc}}(\mathbf{x}, \boldsymbol{\xi})$ and the interpolation $w_{\text{disc}}(\mathbf{x}, \boldsymbol{\xi})$ become a function of \mathbf{x} , such that the interpolation step $w_{\text{disc}}(\mathbf{x}, \boldsymbol{\xi}) = \mathcal{I}(\mathbf{v}_{\text{disc}}(\mathbf{x}))$ is also repeated for each \mathbf{x} in the spatial discretization. For a one-dimensional physical space, $r = 1$, the distance reduces to $d_{\text{disc}}(x, \boldsymbol{\xi}) = x_{\text{disc}}(\boldsymbol{\xi}) - x$ such that parameterizing the discontinuity location $x_{\text{disc}}(\boldsymbol{\xi}) = X_{\text{disc}}(\boldsymbol{\xi})$ is sufficient, which is independent of x . If multiple discontinuities are present in the spatial field of $u(x, \boldsymbol{\xi})$ then the subcell resolution algorithm is applied to each physical discontinuity. A non-monotonic function for $w_{\text{disc}}(x, \boldsymbol{\xi})$ also results in multiple discontinuities in $w(x, \boldsymbol{\xi})$ at certain values of x .

At physical points x where the hypersurface $\Xi_{\text{disc}}(x)$ is located close to the boundary of the parameter space Ξ , no simplexes Ξ_i may lie entirely in the region on one side of $\Xi_{\text{disc}}(x)$. For instance, Ξ^- might not contain any simplexes Ξ_{i-} for updating the interpolation $w_j^-(x, \boldsymbol{\xi})$ to $w_{i-}(x, \boldsymbol{\xi})$ in $\Xi_j^-(x)$ of the simplex Ξ_j that contains $\Xi_{\text{disc}}(x)$. In that case, a constant function is used for $w_j^-(x, \boldsymbol{\xi})$. The constant value for $w_j^-(x, \boldsymbol{\xi})$ is the arithmetic average of the samples $v_k(x)$ at the vertexes of Ξ_j in Ξ_j^- . In any other cases, the interpolation $w_j(x, \boldsymbol{\xi})$ (2) is simply retained.

2.4 Monotonicity preserving limiter

The MP limiter combines the monotonicity of the approximation at discontinuities with higher-degree interpolation at smooth local extrema through a three-step implementation. The first step is the replacement of the LEC condition Eq. (3) with an MP condition in the interior of the simplexes Ξ_j , since Eq. (3) does not necessarily result in a monotonic interpolation in Ξ_j as long as no artificial extrema exceed the sampled values \mathbf{v}_j . This

requirement is enforced by making a Delaunay sub-tessellation in Ξ_j of the vertexes ξ_k of Ξ_j and the Monte Carlo (MC) points ξ_{mc_k} in Ξ_j for integrating $w(\mathbf{x}, \xi)$. If the value $w(\mathbf{x}, \xi_{mc_k})$ at any of the MC points ξ_{mc_k} of this simplex sub-triangulation in Ξ_j is larger or smaller than the value at all other vertexes of all sub-simplexes of which ξ_{mc_k} is a vertex, then the interpolation $w_j(\mathbf{x}, \xi)$ is non-monotonic. The polynomial degree $p_j(\mathbf{x})$ and the stencil $S_j(\mathbf{x})$ of Ξ_j are then reduced similarly as for the LEC limiter. This MP criterion is more restrictive than that of the LEC version, and it is always satisfied for a reduction to $p_j(\mathbf{x}) = 1$.

The second part is to turn off the MP limiter at local extrema in the solution, since at these locations there is no monotonicity in the response that can be preserved. This is the stochastic equivalent of the MP limiter for FVM in the physical space by [7] in the sense that it deactivates the limiter at local extrema. These extrema in $u(\mathbf{x}, \xi)$ are identified by local extrema in the samples \mathbf{v} in the interior of Ξ , since $u(\mathbf{x}, \xi)$ has a local extremum if $v_k(\mathbf{x})$ is also a local extremum. A local extremum at ξ_k is again detected if $v_k(\mathbf{x})$ is larger or smaller than the samples in all other vertexes of all simplexes that contain ξ_k . If $v_k(\mathbf{x})$ is such a local extremum, then the MP limiter is deactivated in all simplexes of which ξ_k is a vertex.

In order to avoid overshoots, it is important to turn the MP limiter off only at smooth extrema in the solution and not for extrema at discontinuities. The gradient magnitude of a linear interpolation in Ξ_j is used in the third step to detect the latter non-smooth extrema. If the gradient in any of the simplexes that contain the local extremum ξ_k surpasses a threshold value, then ξ_k is not treated as a smooth extremum and the MP limiter is retained in all simplexes that contain the vertex ξ_k . The second formulation of the MP limiter in FVM by [10] based on enlarging the limiter intervals will be extended in future work, since it is expected to give equally robust results without the sensitivity to a threshold parameter.

3.0 RESULTS

3.1 Shock tube problem

The shock tube problem involves Sod's Riemann problem for the Euler equations of one-dimensional unsteady inviscid flow without heat conduction. The governing system of hyperbolic equations is given in conservation formulation by

$$\frac{\partial U}{\partial t} + \frac{\partial F(U)}{\partial x} = 0, \quad (12)$$

with the state vector $U(x, t)$ and flux vector $F(x, t)$

$$U = \begin{pmatrix} \rho \\ \rho u \\ \rho E \end{pmatrix}, \quad F = \begin{pmatrix} \rho u \\ \rho u^2 + p \\ \rho u H \end{pmatrix}, \quad (13)$$

and initial conditions $U(x, 0) = U_0(x)$. For a perfect gas, the density $\rho(x, t)$, velocity $u(x, t)$, static pressure $p(x, t)$, total energy $E(x, t)$, and enthalpy $H(x, t)$ are related as $E = (1/(\gamma - 1))p/\rho + u^2/2$ and $H = E + p/\rho$, with ratio of specific heats $\gamma = c_p/c_v$. Sod's Riemann problem is characterized by the initial conditions $U_0(x)$ consisting of two uniform states at the left and the right of $x_0 = 0$

$$\begin{cases} u_{\text{left}} = 0, \\ p_{\text{left}} = 1, \\ \rho_{\text{left}} = 1, \end{cases} \quad \begin{cases} u_{\text{right}} = 0, \\ p_{\text{right}} = 0.1, \\ \rho_{\text{right}} = 0.125. \end{cases} \quad (14)$$

The pressure p_{left} of the initial left state and the location x_0 of the initial discontinuity are assumed to be uncertain. The uncertainty is given by two uniform distributions on the domains $p_{\text{left}} \in [0.9; 1.1]$ and $x_0 \in$

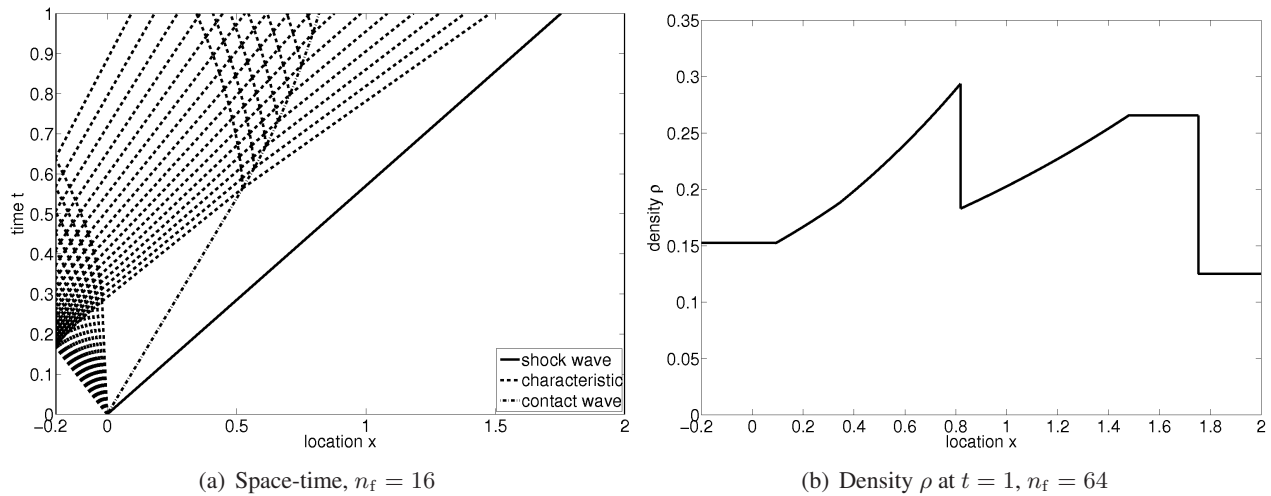


Figure 6: Sod's Riemann problem in a closed shock tube with deterministic initial conditions.

$[-0.025; 0.025]$. The output quantities of interest are the density ρ at $x = 0.82$ and on the entire spatial domain. The problem is here confined to a closed shock tube on a finite spatial domain $x \in [-0.2; 2]$ with reflective walls at the boundaries, as considered deterministically in [11]. The Euler equations (12) are solved up to $t = 1$ using a second order front tracking method [11], which tracks the location of waves in the flow solution and solves local Riemann problems to simulate their interactions. It resolves shock waves and contact surfaces as true discontinuities unaffected by numerical diffusion, which results in sharp jumps in the physical and probability spaces. Rarefaction waves are discretized by a series of characteristics and second order convergence is obtained using a piecewise linear reconstruction of the rarefaction wave solution. Based on a convergence study, the rarefaction wave is here discretized using $n_f = 64$ characteristic fronts.

The space–time solution of the deterministic problem is shown in Figure 6(a) in terms of the wave paths for $n_f = 16$. A left running rarefaction wave, a contact discontinuity, and a right running shock wave emanate from the discontinuity in the initial conditions at $x_0 = 0$. The rarefaction wave reflects from the left boundary and interacts with the contact discontinuity in the interior of the domain. The corresponding profile of the density ρ at $t = 1$ is given in Figure 6(b) for $n_f = 64$. Next to the shock wave, the contact surface also results in a discontinuity and three points with a discontinuous derivative in the density field.

The uncertainty in p_{left} and x_0 leads to a jump in the response surface for the density ρ at an x -location near the contact discontinuity, $x = 0.82$. The SSC discretization of the two-dimensional probability space is shown in Figure 7(a) in terms of the tessellation of $n_s = 100$ sampling points. The adaptive refinement algorithm clusters the sampling points near the discontinuity that runs diagonally through the probability space. The SSC–ENO method obtains a significantly higher density of the sampling points near the jump in Figure 7(b) for the same number of samples. This results in a sharper resolution of the discontinuity and a larger ratio in size between the cells near the singularity and those that discretize the continuous regions. The improved effectiveness of the adaptive refinement is caused by the increase of the local polynomial degree p_j in the smooth cells Ξ_j by the stencil selection and the resulting concentration of the sampling in the cells that contain the discontinuity. SSC–ENO predicts a mean pressure of $\mu_\rho = 0.231$ with a standard deviation of $\sigma_\rho = 0.0543$. The coarser discretization of the discontinuity by SSC leads to an underprediction of the standard deviation with $\sigma_\rho = 0.0534$.

The SSC–ENO response surface approximation for ρ as a function of p_{left} and x_0 with the simplex tes-

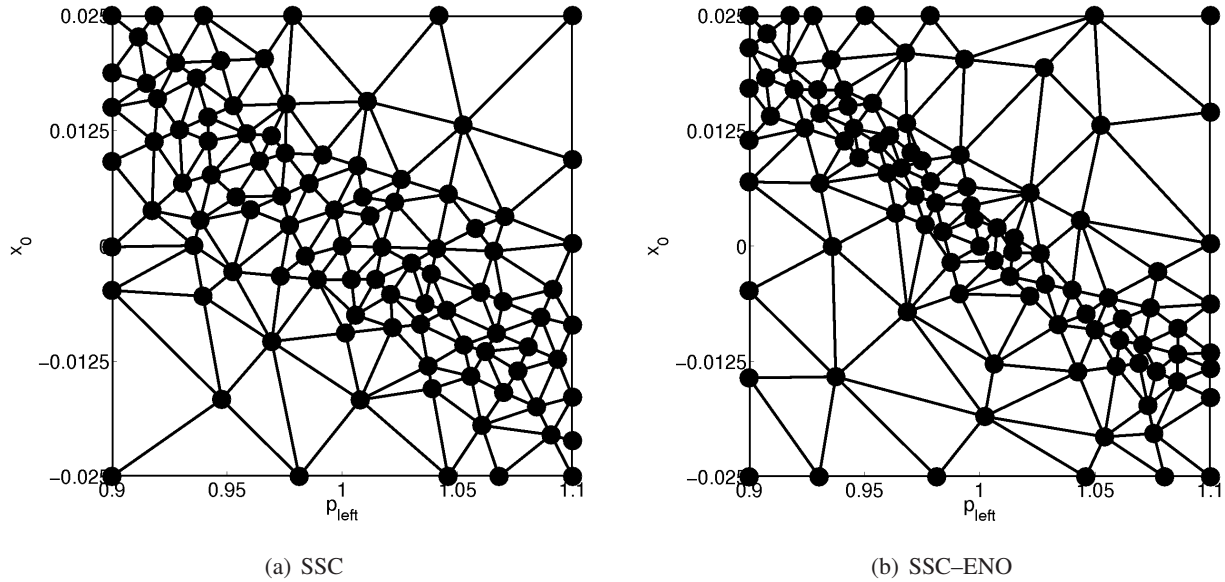


Figure 7: Discretization of the parameter space Ξ for the density ρ at $x = 0.82$ and $t = 1$ with $n_s = 100$ for Sod's Riemann problem in a closed shock tube with uncertain p_{left} and x_0 .

sellation is shown in Figure 8(a). The response shows two continuous regions separated by a discontinuity that varies in strength and that is slightly curved. SSC-ENO gives a robust approximation of the discontinuity without overshoots because of the linear interpolation in the small simplexes that contain the singularity. Nevertheless, the subcell resolution of the SSC-SR method already achieves a more accurate response surface approximation using uniform sampling with only $n_s = 15$ samples in Figure 8(b). The jump is captured as a true discontinuity by extrapolating the interpolations $w_j(\xi)$ from both sides into the discontinuous cells up to the predicted singularity location. This leads to a piecewise higher-degree approximation that resolves the two smooth regions and the curved discontinuity of varying strength in between.

The discontinuity location is approximated using SSC-SR by interpolating the contact discontinuity locations x_{contact} extracted from the deterministic simulations, as shown in Figure 9. The interpolation of x_{contact} as a function of p_{left} and x_0 is performed using the SSC-ENO algorithm. The resulting jump line for $x = 0.82$ in the (p_{left}, x_0) -plane is then given by the intersection of the surface for x_{contact} with the horizontal plane at $x_{\text{contact}} = 0.82$. The jump line approximation consists of a piecewise higher-order polynomial that is able to capture its curvature. The statistical moments predicted by SSC-SR are $\mu_\rho = 0.231$ and $\sigma_\rho = 0.0557$. The mean value matches that of SSC-ENO, but the standard deviation is underpredicted by SSC-ENO because of the linear approximation of the discontinuity. It corresponds to an output coefficient of variation of $\text{CoV}_\rho = 24.1\%$.

The output uncertainty in the entire density profile on $x \in [-0.2; 2]$ is depicted in Figures 10 and 11 in terms of the convergence for the mean $\mu_\rho(x)$ and the standard deviation $\sigma_\rho(x)$ of SSC-ENO with $n_s = \{10, 20, 100\}$ and SSC-SR with $n_s = \{10, 15, 20\}$. The mean density $\mu_\rho(x)$ shows the smearing of the shock and contact waves compared to the deterministic solution, which is caused by the random location of the discontinuities. This also produces the local maxima of the standard deviation $\sigma_\rho(x)$ in the discontinuous regions. The results for SSC-SR are indistinguishable and converged to a maximum standard deviation of $\sigma_{\rho, \text{max}} = 0.0730$ at $x = 1.754$ for $n_s = 15$.

Non-intrusive uncertainty quantification

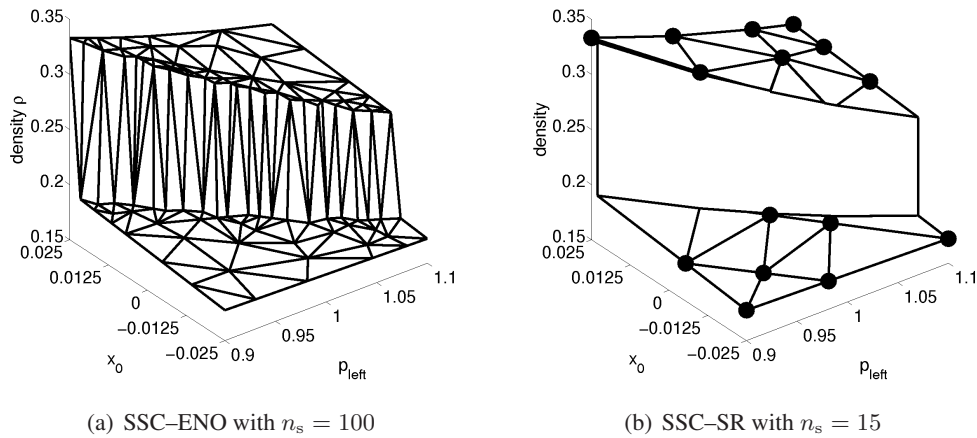


Figure 8: Response surface approximations for the density ρ at $x = 0.82$ and $t = 1$ for Sod's Riemann problem in a closed shock tube with uncertain p_{left} and x_0 .

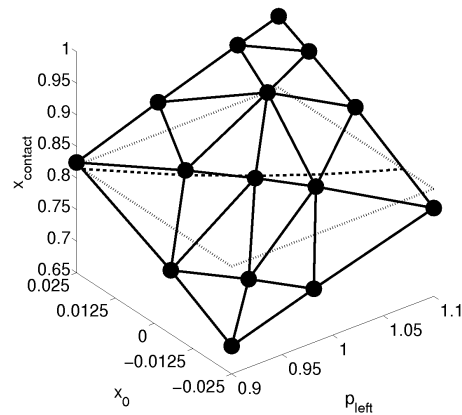


Figure 9: SSC-SR response surface approximation for the contact discontinuity location x_{contact} at $t = 1$ with $n_s = 15$ for Sod's Riemann problem in a closed shock tube with uncertain p_{left} and x_0 .

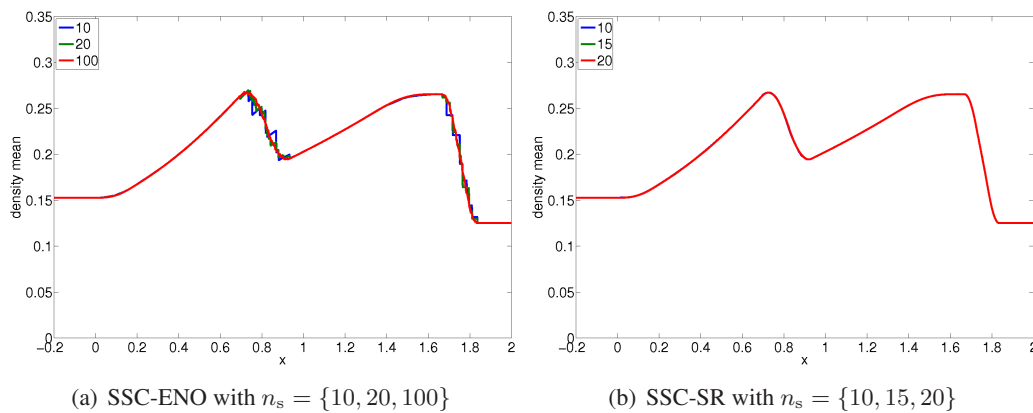


Figure 10: Mean $\mu_\rho(x)$ of the density ρ for Sod's Riemann problem in a closed shock tube with uncertain initial pressure p_{left} and diaphragm location x_0 .

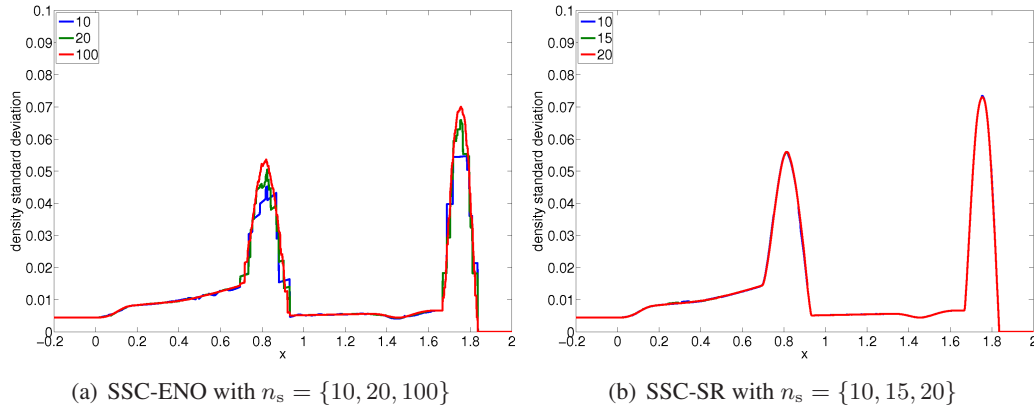


Figure 11: Standard deviation $\sigma_\rho(x)$ of the density ρ for Sod's Riemann problem in a closed shock tube with uncertain initial pressure p_{left} and diaphragm location x_0 .

SSC-ENO results in a staircase approximation in the discontinuous regions. With an increasing number of samples, the solution converges to a smooth representation with a larger number of smaller jumps. However, due to the absence of viscosity in the physical problem, the approximation maintains a staircase character which leads to first-order accuracy. It also results in the convergence to the maximum standard deviation from below which causes an underprediction of the maximum standard deviation at underresolved sample sizes. It leads to an underprediction of the maximum output uncertainty with $\sigma_{\rho, \text{max}} = 0.0700$ by 4.16% even for $n_s = 100$. Refinement measure $\bar{\Xi}_j$ is used here for SSC-ENO, since the discontinuities have different locations in probability space for each spatial point x .

3.2 Transonic airfoil

3.2.1 Inviscid flow

Non-uniform probability distributions are considered in a FVM discretization of multiple spatial dimensions for the transonic flow over the RAE 2822 airfoil. The randomness in this NODESIM-CFD test case is given by independent normal distributions for the free-stream Mach number M_∞ and the angle of attack α with the mean values 0.734 and 2.79° , and standard deviations 0.005 and 0.1° , respectively. The flow problem is solved using an upwind discretization of the inviscid Euler equations in *FLUENT* to obtain a sharp discontinuity in the flow field up to the pressure distribution on the airfoil surface. The deterministic results for the two-dimensional spatial discretization with $5 \cdot 10^4$ cells are shown in Figure 12 in terms of the static pressure field around the airfoil and the distribution of the pressure coefficient C_p over the surface

$$C_p = \frac{p - p_\infty}{\frac{1}{2} \rho_\infty u_\infty^2}, \quad (15)$$

where the subscript ∞ denotes the free-stream conditions of the pressure, the density, and the velocity. A transonic shock wave forms above the airfoil, which results in a discontinuity in the surface pressure distribution. The undershoot downstream of the shock wave is caused by the expansion present after an inviscid shock in a transonic flow.

The shock location x_{shock} along the airfoil is parameterized by SSC-SR for resolving the stochastic surface pressure distribution. The shock sensor of Harten [6] is used to extract x_{shock} from each of the samples, based

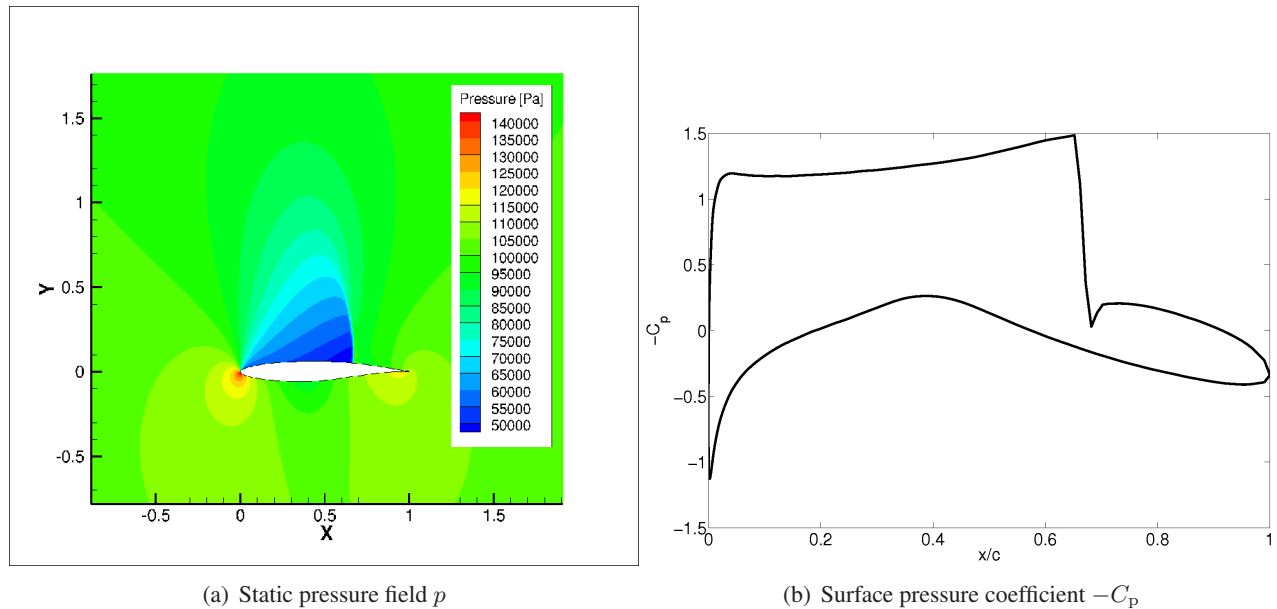


Figure 12: Deterministic results for the transonic flow over the RAE 2822 airfoil.

on the maximum of the gradient magnitude of the pressure coefficient $|dC_p/dx|$ in the shock region. A discrete resolution of the shock location, limited to the spatial cell faces, is avoided by defining x_{shock} as the extremum of a parabolic fit through the maximum of $|dC_p/dx|$ and the values at its two neighboring spatial points. The extraction step \mathcal{E} is repeated on each layer of cells above the airfoil to obtain the two-dimensional shape of the shock wave X_{shock} for resolving the stochastic pressure field.

The standard deviation of the pressure coefficient $\sigma_{C_p}(x)$ along the upper surface in Figure 13 is significantly underpredicted in the shock region by SSC-ENO with a maximum of $\sigma_{C_p, \text{max}} = 0.362$ for $n_s = 50$. It converges only slowly to the SSC-SR solution of $\sigma_{C_p, \text{max}} = 0.616$ at $n_s = 50$, which corresponds to an underprediction by 41.2%. Convergence is therefore not established with this method for $n_s = 50$. In contrast, the SSC-SR method already gives an accurate prediction for only $n_s = 5$ samples that largely coincides with the approximation of $n_s = 50$. On the other hand, the region around the shock wave in which $\sigma_{C_p}(x)$ is elevated is overpredicted by SSC-ENO. Both effects are caused by the underresolution of the discontinuity in the probability space by the piecewise linear approximation of the discontinuity by SSC-ENO. The linear function leads to a lower standard deviation through the underprediction of the gradients in the response surface and to a longer shock region through the smearing of the discontinuity in the probability space. The normal input distributions increase these two effects due to the concentration of the probability in a small region of the probability space, which makes the sharp resolution of the discontinuity in that region even more important.

The standard deviation $\sigma_p(x, y)$ of the pressure field around the RAE 2822 airfoil is given in Figure 14 for SSC-ENO and SSC-SR with $n_s = 5$ samples, which correspond on the upper surface with the results of Figure 13. For this minimal number of samples of $n_s = 5$, SSC-SR also captures already the detailed spatial structure of the local standard deviation field $\sigma_p(x, y)$, while SSC-ENO gives a qualitative indication of the region with increased values of $\sigma_p(x, y)$ only.

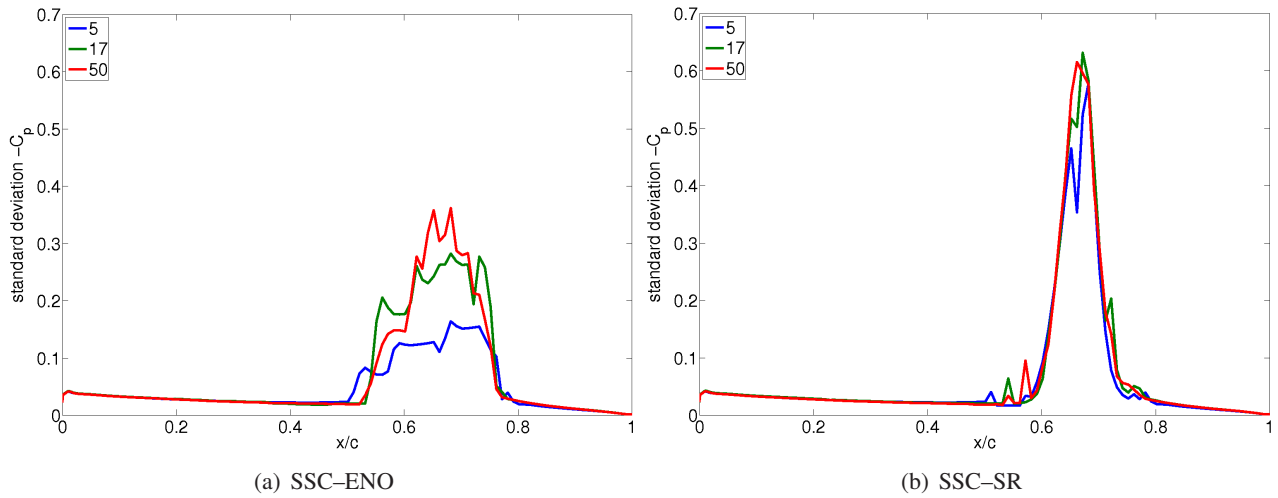


Figure 13: Standard deviation of the pressure coefficient $\sigma_{C_p}(x)$ along the surface with $n_s = \{5, 17, 50\}$ for the transonic flow over the RAE 2822 airfoil with random free-stream Mach number M_∞ and angle of attack α .

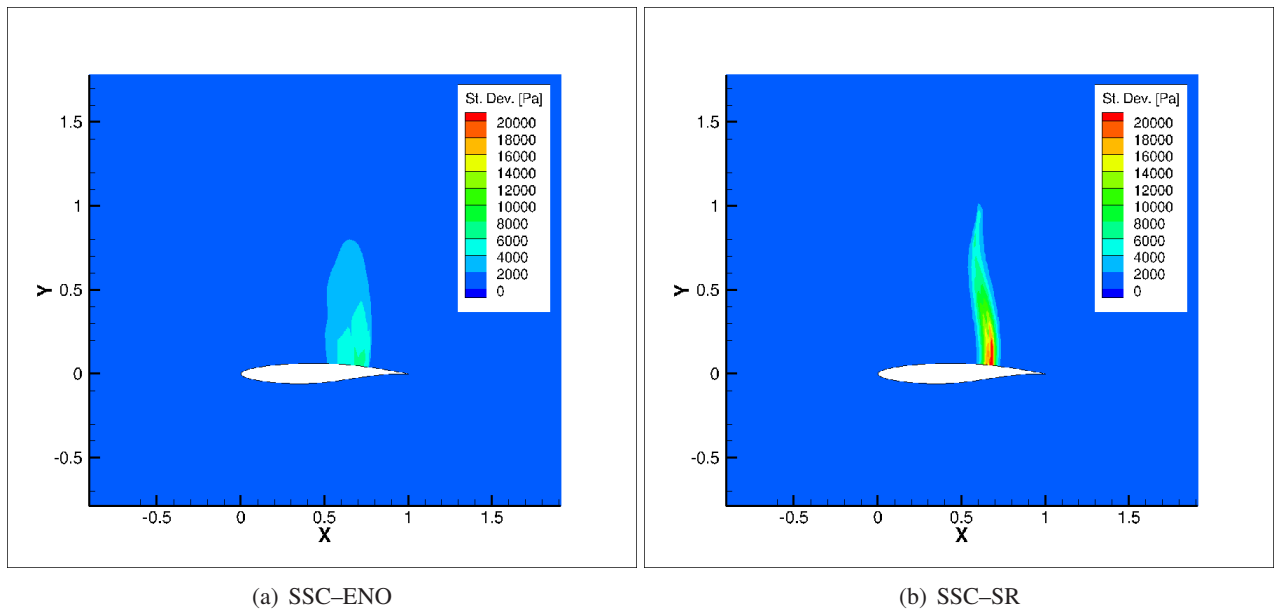


Figure 14: Standard deviation of the pressure field $\sigma_p(x, y)$ with $n_s = 5$ for the transonic flow over the RAE 2822 airfoil with random free-stream Mach number M_∞ and angle of attack α .

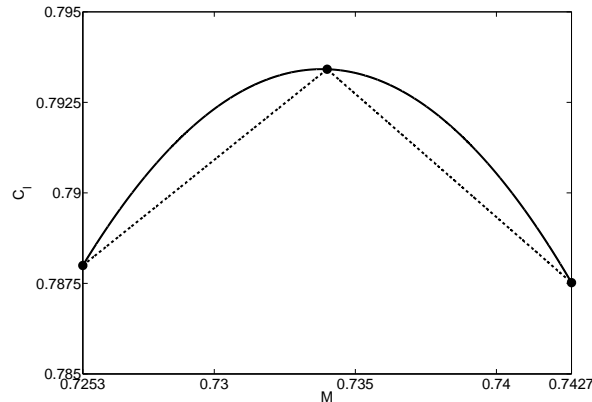


Figure 15: Response surface approximation of C_1 as a function of M by the LEC and MP limiters for the transonic flow over the RAE 2822 airfoil with $n_s = 3$.

Table 1: Convergence of μ_{C_1} by the LEC and MP limiters for the transonic flow over the RAE 2822 airfoil.

n_s	LEC	MP
3	$7.9059 \cdot 10^{-1}$	$7.9153 \cdot 10^{-1}$
5	$7.9117 \cdot 10^{-1}$	$7.9115 \cdot 10^{-1}$
9	$7.9131 \cdot 10^{-1}$	$7.9139 \cdot 10^{-1}$

3.2.2 Viscous flow

The lift coefficient C_1 has a non-monotonic dependence on the Mach number M in the standard transonic flow problem around the RAE 2822 airfoil. The uniform distribution for M is defined by a mean of $\mu_M = 0.734$ and standard deviation of $\sigma_M = 0.005$ at an angle of attack of $\alpha = 2.79^\circ$ and a Reynolds number of $Re = 6.5 \cdot 10^6$. The fully turbulent flow problem is solved using the *Fluent* Reynolds-averaged Navier-Stokes solver with the Spalart-Allmaras turbulence model and a second-order Roe upwind discretization on a two-dimensional mesh of $7.5 \cdot 10^4$ spatial cells. The height of the first cell layer above the airfoil is with $1 \cdot 10^{-5}c$ smaller than the y^+ -value of 1 and the dimensions of the mesh are $32.5c \times 25c$, where $c = 1$ is the airfoil chord. Only the pressure forces on the airfoil are taken into account in computing C_1 .

Approximation of the non-monotonic response surface of C_1 as a function of M is shown in Figure 15 for the initial discretization of the LEC and MP limiters with $n_s = 3$. The quadratic interpolation through the samples for the MP limiter already leads to a more realistic representation of the dependence of C_1 on M . The LEC limiter gives a piecewise linear approximation because the sampling point at the nominal condition $M = 0.734$ is not exactly located at the maximum of C_1 . This results initially for $n_s = 3$ in an underprediction of the mean lift coefficient μ_{C_1} for the LEC limiter, as demonstrated by the convergence in Table 1. The mean and standard deviation of the drag and pitching moment coefficients, C_d and C_m , respectively, are given in Table 2 for the MP limiter with $n_s = 9$. Both C_d and C_m depend monotonically on M such that the LEC results are identical. The drag coefficient C_d has the highest coefficient of variation with $CoV_{C_d} = 14.9\%$, and C_1 is relatively the least sensitive to variations in M with $CoV_{C_1} = 0.204\%$ because of the non-monotonicity of its response surface.

Table 2: Mean μ , standard deviation σ , and coefficient of variation CoV of the lift, drag, and pitching moment coefficients by the MP limiter for the transonic flow over the RAE 2822 airfoil with $n_s = 9$.

	μ	σ	CoV
C_l	$7.9139 \cdot 10^{-1}$	$1.6140 \cdot 10^{-3}$	$2.0395 \cdot 10^{-3}$
C_d	$1.4710 \cdot 10^{-2}$	$2.1910 \cdot 10^{-3}$	$1.4895 \cdot 10^{-1}$
C_m	$9.8398 \cdot 10^{-2}$	$3.4812 \cdot 10^{-3}$	$3.5379 \cdot 10^{-2}$

4.0 CONCLUSIONS

The Simplex Stochastic Collocation (SSC) method obtains robust and non-intrusive solutions of uncertainty quantification problems in computational fluid dynamics. It is based on a simplex tessellation discretization of the probability space and piecewise polynomial interpolation of higher-degree stencils of samples at the vertexes of the simplexes.

Essentially Non-Oscillatory (ENO) type stencil selection is introduced into the SSC method to achieve an accurate approximation of discontinuities in probability space. The stencil selection for simplex Ξ_j chooses the stencil S_j with the highest polynomial degree p_j that is accepted by the Local Extremum Conserving (LEC) limiter. This results in an increase of the local polynomial degree in the smooth regions and a concentration of the refinement in the simplexes that contain the discontinuity. The efficient implementation of the algorithm assigns only nearest neighbor stencils to other simplexes without constructing new stencils or interpolations.

A subcell resolution approach is also introduced into the SSC method for solving stochastic problems with randomness in the location of spatial discontinuities. The presented SSC–SR method is based on extracting the discontinuity location $X_{\text{disc}}(\xi)$ in the physical space from each of the deterministic solutions. The realizations of the physical distance $d_{\text{disc}}(\mathbf{x}, \xi)$ to the discontinuity $X_{\text{disc}}(\xi)$ are interpolated over the stochastic dimensions to predict the location of the discontinuity $\Xi_{\text{disc}}(\mathbf{x})$ in the probability space. The stochastic response surface approximations are then extended from both sides up to the discontinuous hypersurface $\Xi_{\text{disc}}(x)$. This results in a truly discontinuous representation of random spatial discontinuities in the interior of the cells discretizing the stochastic dimensions.

The LEC limiter reduces the polynomial interpolation degree to a piecewise linear function at smooth local extrema in the response surface. Therefore, the MP limiter is introduced into UQ to combine a higher-degree approximation of smooth non-monotonic solutions with a non-oscillatory interpolation at discontinuities.

The uncertainty in the shock tube problem results in an output coefficient of variation for the density of 23.5% in the interaction region of the contact and rarefaction wave. The large and asymmetrical uncertainty intervals, near the smeared discontinuities in the mean sense, indicate a robust approximation of the highly nonlinear propagation of the uncertainty in those regions. SSC–SR results in a converged solution for $n_s = 15$ samples compared to an underprediction of the maximum standard deviation $\sigma_{\rho, \text{max}}$ by 4.16% for SSC–ENO with $n_s = 100$.

The impact of the random free-stream conditions on the transonic flow around the RAE 2822 airfoil are accurately resolved in the surface pressure distribution, and the mean and standard deviation pressure fields for a minimal number of $n_s = 5$ samples. The non-uniform input probability distributions lead to an even more significant underprediction of $\sigma_{C_p, \text{max}}$ by 41.2% for SSC–ENO with $n_s = 50$. The MP limiter enables us to accurately resolve the non-monotonic response of the lift coefficient C_l as a function of the random Mach number for the RAE2822 transonic airfoil. This reveals that C_l is less sensitive to the uncertainty owing to the non-monotonicity of the response surface compared to the drag and moment coefficients C_d and C_m with monotonic responses.

ACKNOWLEDGMENTS

I would like to acknowledge Prof. Gianluca Iaccarino for his contributions to [12–15].

REFERENCES

- [1] R. Abgrall, P.M. Congedo, A semi-intrusive deterministic approach to uncertainty quantification in non-linear fluid flow problems, *Journal of Computational Physics* **235** (2013) 828–845.
- [2] T. Barth, On the propagation of statistical model parameter uncertainty in CFD calculations, *Theor. Comput. Fluid Dyn.* **26** (2012) 435–457.
- [3] R.G. Ghanem, P.D. Spanos, *Stochastic Finite Elements: A Spectral Approach*, Springer–Verlag, New York (1991).
- [4] D. Ghosh, R. Ghanem, Stochastic convergence acceleration through basis enrichment of polynomial chaos expansions, *Int. J. Numer. Meth. Eng.* **73** (2008) 162–184.
- [5] A. Harten, S. Osher, Uniformly high-order accurate nonoscillatory schemes I, *SIAM J. Numer. Anal.* **24** (1987) 279–309.
- [6] A. Harten, ENO schemes with subcell resolution, *J. Comput. Phys.* **83** (1989) 148–184.
- [7] B.P. Leonard, A.P. Lock, M.K. Macvean, The NIRVANA scheme applied to one-dimensional advection, *International Journal of Numerical Methods for Heat and Fluid Flow* **5** (1995) 341–377.
- [8] O.P. Le Maître, H.N. Najm, R.G. Ghanem, O.M. Knio, Multi-resolution analysis of Wiener-type uncertainty propagation schemes, *J. Comput. Phys.* **197** (2004) 502–531.
- [9] C.-W. Shu, S. Osher, Efficient implementation of essentially non-oscillatory shock-capturing schemes II, *J. Comput. Phys.* **83** (1989) 32–78.
- [10] A. Suresh, H.T. Huynh, Accurate monotonicity-preserving schemes with Runge-Kutta time stepping, *Journal of Computational Physics* **136** (1997) 83–99.
- [11] J.A.S. Witteveen, Second order front tracking for the Euler equations, *J. Comput. Phys.* **229** (2010) 2719–2739.
- [12] J.A.S. Witteveen, G. Iaccarino, Simplex stochastic collocation with random sampling and extrapolation for nonhypercube probability spaces, *SIAM J. Sci. Comput.* **34** (2012) A814–A838.
- [13] J.A.S. Witteveen, G. Iaccarino, Refinement criteria for simplex stochastic collocation with local extremum diminishing robustness, *SIAM J. Sci. Comput.* **34** (2012) A1522–A1543.
- [14] J.A.S. Witteveen, G. Iaccarino, Simplex stochastic collocation with ENO-type stencil selection for robust uncertainty quantification, *J. Comput. Phys.*, **239** (2013) 1–21.
- [15] J.A.S. Witteveen, G. Iaccarino, Subcell resolution in simplex stochastic collocation for spatial discontinuities, *J. Comput. Phys.*, **251** (2013) 17–52.
- [16] D. Xiu, J.S. Hesthaven, High-order collocation methods for differential equations with random inputs, *SIAM J. Sci. Comput.* **27** (2005) 1118–1139.